

Synthesis and sintering of (Mg, Co, Ni, Cu, Zn)O entropy-stabilized oxides obtained by wet chemical methods

Mattia Biesuz^{1,2,#} ORCID: 0000-0002-4338-4177

Luca Spiridigliozzi³, ORCID: 0000-0002-0788-4190

Gianfranco Dell'Agli³, ORCID: 0000-0001-7690-846X

Mauro Bortolotti¹, ORCID: 0000-0002-7213-6316

Vincenzo M. Sglavo^{1,2} ORCID: 0000-0001-9133-7204

¹ University of Trento, Department of Industrial Engineering

Via Sommarive 9,

38123 Trento –ITALY–

² INSTM, Research Unit of Trento

Via G. Giusti 9,

50121 Firenze –ITALY–

³ University of Cassino and Southern Lazio, Department of Civil and Mechanical Engineering,

Via Di Biasio 43,

03043 Cassino (FR) –ITALY–

Corresponding Author: mattia.biesuz@unitn.it

Keyword: entropy stabilized oxides; sintering; co-precipitation; hydrothermal synthesis; ceramics

Published version available at

<https://link.springer.com/article/10.1007/s10853-018-2168-9>

Abstract

Entropy-stabilized oxides represent a novel family of advanced ceramic materials with attractive functional properties.

In this work, entropy-stabilized oxides, in the system (Mg, Co, Ni, Cu, Zn)O, were produced by co-precipitation and hydrothermal synthesis. Although TG/DTA and XRD analyses of as-synthesized powders point out complex thermal evolution, in both cases the desired single-phase rock salt solid solution was obtained after a proper thermal treatment.

The dilatometric analysis points out the excellent sinterability of the obtained powders, which were successfully consolidated for the first time reaching nearly full density ($\sim 97\%$) at relatively low temperature (1050°C).

1 Introduction

Entropy-Stabilized Oxides (E-SO) are a new class of ceramic materials characterized by very promising and still partially unexplored functional properties^{1–5}. They were synthesized for the first time by Rost et al. in 2015 [1] by mixing five equimolar metal oxides (MgO-CoO-NiO-CuO-ZnO), the powder mixture being heat treated at 1000°C and then quenched. At such temperature the oxides mixture reacts forming a single phase solid solution with *rock salt* crystalline structure (Mg_{0.2}Co_{0.2}Ni_{0.2}Cu_{0.2}Zn_{0.2}O)[1] which is thermodynamically stabilized by the mixing entropic contribution (ΔS_{mix}) to the Gibbs free energy [1, 6]:

$$\Delta G_{mix} = \Delta H_{mix} - T \Delta S_{mix} = \Delta H_{mix} + RT \sum_{i=1}^n x_i \ln(x_i) \quad \text{Eq. 1}$$

where T is the absolute temperature, ΔG_{mix} and ΔH_{mix} the free energy and enthalpy of mixing, respectively, R the universal gas constant and x_i the molar concentration of each component of the mixture. ΔS_{mix} is always positive and, therefore, the rock salt single-phase stability increases

with temperature. Rost et al. pointed out that for temperature in excess to 875°C the solid solution of the equimolar MgO-CoO-NiO-CuO-ZnO system is more stable than the separated oxides. Therefore, slow cooling or annealing at temperature below 875°C causes phase separation via exsolution. But, if the cooling rate is high enough (quenching), the metastable elevated temperature rock salt single-phase can be stabilized down to room temperature.

The work by Rost et al. opened a new broad materials research field, pointing out how to produce new complex materials with virtually infinite different compositions and properties. Basically, the idea can be applied to different classes of inorganic materials, thus allowing the production of highly disordered new crystalline phases. Similar works were focused on the production of entropy-stabilized carbides, carbo-nitrides and borides [7–9]. Recently, new E-SO were developed with compositions different from the equimolar (Mg, Co, Ni, Cu, Zn)O[10–12]. In particular, Bérardan and co-workers showed that (Mg, Co, Ni, Cu, Zn)O can be easily doped with alkali metal oxides, i.e. Li₂O, Na₂O and K₂O[10]. They were able to obtain single phase rock salt (Mg, Co, Ni, Cu, Zn)_{1-x}Li_xO with x up to ~ 0.3. Such materials are characterized by interesting electrical properties like room temperature superionic Li⁺ and fast Na⁺ conductivity [10] and giant dielectric constant[12], suggesting possible applications in the field of energy storage and microelectronics.

Although E-SO represent a very promising innovative class of ceramics, no works have been carried out to investigate their consolidation and densification processes. In some works E-SO manufactured by conventional solid state synthesis route were used to produce pellets for electrical properties measurements, but their relative density did not exceed 75-80% [5, 10, 12].

Finally, it must be pointed out that solid state synthesis route requires a homogeneous distribution of the different oxides particles prior to the high temperature treatment. Therefore, very long ball-milling is necessary before starting the synthesis process.

Recently, Sarkar et al. have shown that different chemical synthesis routes allow the production of nanometric E-SO powder in the system (Mg, Co, Ni, Cu, Zn)O [13]; among them, flame spray pyrolysis, nebulized spray pyrolysis and co-precipitation, using NH_3 as precipitating agent.

In this work, a processing route based on wet chemical synthesis procedures (co-precipitation and hydrothermal synthesis) was developed to obtain (Mg, Co, Ni, Cu, Zn)O entropy-stabilized nanometric oxides which allows the production of almost fully dense ceramic components by sintering at relatively low temperature.

2 Experimental procedures

Zinc (II) sulphate ($\text{ZnSO}_4 \cdot \text{H}_2\text{O}$ RPE, Carlo Erba Reagents), copper (II) sulphate ($\text{CuSO}_4 \cdot 5\text{H}_2\text{O}$ RPE, Carlo Erba Reagents), nickel (II) sulphate ($\text{NiSO}_4 \cdot 5\text{H}_2\text{O}$ RPE, Carlo Erba Reagents), cobalt (II) nitrate ($\text{Co}(\text{NO}_3)_2 \cdot 5\text{H}_2\text{O}$ RPE, Carlo Erba Reagents) and magnesium (II) nitrate ($\text{Mg}(\text{NO}_3)_2 \cdot 5\text{H}_2\text{O}$ RPE, Carlo Erba Reagents) were used as precursors for preparing the aqueous solutions used in the present work. Two different wet synthesis methods were adopted, a simple co-precipitation method and a combined co-precipitation/hydrothermal treatment synthesis. Potassium carbonate (K_2CO_3 , RPE, Carlo Erba Reagents) and sodium hydroxide (NaOH , RPE, Carlo Erba Reagents) were used as precipitating/mineralizer agent in the two cases, respectively. These products were chosen as precipitating agents after some preliminary experiments, where the coprecipitation in the presence of ammonia appeared rather difficult to be completed, due to the formation of ammonia complexes (Ni and Cu only partially precipitate). Moreover, precipitating agents based on carbonates, typically produce weakly agglomerated powder which exhibits better sintering [14].

Initially, the proper amount of salts was dissolved in de-ionized water to obtain a first solution (A) with 0.1 M total cationic concentration (0.02 M for each cation). K_2CO_3 was dissolved in de-ionized water to form 0.15 M solution (B). The co-precipitation was carried out in reverse mode, i.e. by

slowly adding solution A to solution B. In a typical synthesis, 400 ml solution A were added at a rate of about 20 ml/min to 400 ml solution B under vigorous stirring. The mix was kept under continuous stirring for 30 min and, finally, the gelatinous co-precipitate was filtered, repeatedly washed with de-ionized water and dried overnight at 60°C. This sample was labeled as CP.

In a typical combined co-precipitation/hydrothermal synthesis route, 40 ml of solution A were quickly added to 10 ml 1.2 M NaOH solution in a Teflon vessel (60 ml), kept under stirring, to induce the formation of a co-precipitated. The Teflon vessel was then sealed and placed in stainless steel pressure vessel for the hydrothermal treatment, which was carried out for 2 days in air-thermostated rotating (25 rpm) oven at 130°C to allow the complete system homogenization. After the hydrothermal treatment, the product was filtered, repeatedly washed with de-ionized water and dried overnight at 60°C. This sample was labeled as HT.

The thermal behavior of CP and HT powders was analyzed by simultaneous Differential Thermal Analysis and Thermo-Gravimetric Analysis (DTA-TG) both in air and in argon atmosphere, using α -Al₂O₃ as reference (Thermoanalyzer STA 409, Netzsch) and 10°C/min heating rate. Additional DTA analysis was performed in air by using different heating rates between 2°C/min and 40°C/min.

In order to understand the complex thermal evolution of the systems, mineralogical analysis was carried out by XRD (Panalytical X'PERT MPD diffractometer, Cu K α radiation) on CP and HT powders. The spectra were collected on samples heat treated at different temperature (from room temperature up to 1000°C) selected on the basis of the thermal effects visible on DTA-TG plots. The heat treatments were carried out in a Lenton chamber furnace under static air atmosphere using heating rate of 10°C/min; once the maximum temperature was reached, the samples were immediately air quenched. The mineralogical composition and the microstructural features (i.e. lattice strain, crystallite size...) were determined by quantitative Rietveld analysis as implemented in Maud software [15].

The relative cations concentration in CP and HT samples was measured by ICP (Spectro Ciros). About 0.15 g of powder was dissolved in 20 ml of a 70% nitric acid (Sigma Aldrich) water solution. This was diluted using 80 ml distilled water to reach 100 ml total volume and then used for the ICP measurements. Two distinct samples were analyzed for CP and HT powders and the analysis was repeated three times on each sample.

The sintering behavior of CP and HT powders was also investigated. As-synthesized powders were preliminarily calcined at 450°C for 1 h (heating rate = 10°C/min) to allow the complete evolution of water. Cylindrical pellets (diameter ~ 6 mm) were produced by uniaxial pressing at 250 MPa. Dilatometric tests were carried out in Linseis L75 dilatometer using heating rate of 10°C/min up to 1100°C. Additional samples were sintered at 1050°C for 1.5 h in Nabertherm muffle under static air atmosphere using 10°C/min heating rate. After firing, the samples were air-quenched by quickly removing them from the furnace.

The microstructure of fired specimens was characterized by SEM (Jeol JSM 5500); the grain size was determined using the linear intercept method on the free surface of sintered pellets, the measure being repeated 10 times. The density of fired bodies was determined according to Archimedes' principle by using an analytical balance (Gibertini, sensitivity $\pm 0.0001\text{g}$). The measures were repeated on four different samples per each composition.

3 Results and discussion

3.1 Synthesis and thermal evolution

Figure 1 shows the XRD pattern recorded on the synthesized powders. Only some very broad peaks appear for the sample obtained by co-precipitation, this pointing out its nanocrystalline or amorphous structure. Conversely, three specific crystalline phases can be recognized in HT powder, namely Brucite, $\text{Mg}(\text{OH})_2$, (ICDD card N. 86-441), Cobalt oxide Co_3O_4 (ICDD card N. 80-1539) and

Tenorite, CuO, (ICDD card N. 45-937). Nevertheless, the presence of Ni(OH)₂ and ZnO cannot be excluded since their XRD reflexes are partially overlapped with those associated with the other identified phases.

The thermal behavior of the synthesized powders is reported in Figure 2. DTA-TG plots for CP powder are characterized by five main thermal effects upon heating (indicated as α , β , γ , δ and ϵ); conversely, only two effects (ζ and η) appear for the material produced by hydrothermal treatment. The first two effects (α and β) for CP powder take place at about 100 and 315°C and correspond to endothermic peaks paired with consistent weight losses, about 10 and 20 wt% for α and β transformation, respectively. The origin of α effect is very likely the evaporation of residual water; instead, β appears to be related to the evolution of crystallization water and carbon dioxide. As a matter of fact, β transformation takes place within the temperature range where hydroxides and basic carbonates of the different metals used in this work typically decompose [16–22].

HT powder is characterized by a unique thermal effect at low temperature (ζ in Figure 2(b)). This phenomenon takes place at ~ 345°C and it is associated to an endothermic peak and 9-10% weight loss. Since some metal hydroxide are formed during the synthesis procedure (Figure 1), ζ is likely associated to the removal of their crystallization water.

At higher temperature two exothermic peaks (γ at ~ 450°C and δ at ~ 595°C) can be observed in CP powder, not paired with any weight change in the TG plot. To investigate these transformations, XRD spectra were collected after heating the co-precipitated powder at specific temperatures and successive quenching. The results, reported in Figure 3 and Table I, reveal the complex thermal evolution of the system. At 390°C (between β and γ effects) Co₃O₄-like spinel and MgO-like rock salt can be distinguished. The presence of Co₃O₄ spinel points out that cobalt ions, introduced as Co²⁺ in the solution, are partially oxidized to Co³⁺ during the thermal treatment; on the other hand, the absence of diffraction signals from any other phases suggests that the lattices of both compounds could be at least partially substituted with other cations. The material at 390°C is

nanocrystalline, with crystallite size of 7.0 and 3.5 nm for the Co_3O_4 and the MgO-like phases, respectively. At 520°C (between γ and δ effects) Co_3O_4 , MgO, CuO and ZnO phases are detected, this suggesting that γ effect in Figure 2 shall be associated to the crystallization of CuO and ZnO. At this temperature, Co_3O_4 and MgO crystallite size remarkably increases up to 24 and 18 nm, respectively, whereas CuO and ZnO exhibit an almost ideal crystallization. Finally, at 690°C (between δ and ϵ effects) the material is mainly constituted by MgO-like rock salt structure, with smaller amounts of CuO and ZnO. The thermal and slow decomposition of Co_3O_4 into CoO with simultaneous evolution of $\text{O}_{2(g)}$ is very likely the cause of the very gradual weight loss observed in this temperature range by TG (Figure 2(a)). It is interesting to observe that at 690°C the system is already largely composed by the rock salt structure typical of (Mg, Co, Ni, Cu, Zn)O entropy-stabilized oxide. This suggests that the dissolution process in the powders manufactured in the present work starts at temperature lower than the threshold one identified by Rost et al. for complete solubility in solid state-synthesized material around 875°C[1]. Nevertheless, the dissolution at 690°C is only partial and higher temperatures are needed for complete solubilization (Figure 3 and Table I). Indeed, the driving force for the single-phase solid solution formation increases with temperature, it being entropy-driven. The result that a partial dissolution takes place also at temperature lower than 875°C is consistent with XRD patterns reported by Rost et al. [1], where a strong reduction of the secondary phases peaks intensity is observed already between 750 and 800°C.

The origin of the δ exothermic peak is not completely clear. It cannot be accounted for by the spinel decomposition or by the formation of the solid solution in the rock salt phase, these processes being endothermic. It can be probably related to the crystallization of some residual amorphous phase. Finally, one can observe that the DTA plot recorded on HT powder does not show any exothermic effect: HT powder does not undergo to any crystallization upon heating, it being already crystalline after the synthesis process (Figure 1).

In order to investigate γ and δ crystallization effects better, DTA analyses with different heating rates ($\varphi = 2 - 40^\circ\text{C}/\text{min}$) were additionally performed. As shown in Figure 4(a), typical DTA peak displacement associated to phase transformation appears. Therefore, the activation energy for γ and δ transformation can be estimated by using a Kissinger-like analysis [23, 24] according to the equation [23, 24]:

$$\ln(T_p^2/\varphi) = E_a/RT_p + B, \quad \text{Eq. 2}$$

where T_p is the DTA peak temperature in Kelvin degrees, E_a the activation energy of the specific phase transition and B a constant. The interpolation of the experimental data using Eq. 2 is shown in Figure 4(b),(c). One can observe that the plots $\ln(T_p^2/\varphi)$ vs. $1000/T_p$ are linear as predicted by Eq. 2. Therefore, it is possible to estimate the activation energy for the two crystallization processes, equal to 225 and 275 kJ/mol for γ and δ transformation, respectively.

At higher temperature an endothermic effect, associated to a moderate weight loss, is recorded for both materials. Such effect, indicated as ϵ and η in Figure 2, takes place at about 780°C . In order to understand the possible phenomena responsible for such endothermic peaks, the thermal analysis was repeated in Ar atmosphere. The corresponding thermographs, compared to those recorded in air, are shown in Figure 5, DTG representing the derivative of TG. Some remarkable differences can be observed for CP powder (Figure 5(a)). DTA-DTG curves do not point out any relevant weight loss and endothermic effect at 780°C in Ar atmosphere. In other words, ϵ can be observed only in air and this suggests that the phenomenon might be related to the modification of the oxidation state of some cations. As a matter of fact, transition metal monoxides like CoO and NiO are typically characterized by consistent deviation from stoichiometry, due to the oxidation of Co^{2+} and Ni^{2+} to trivalent cations [25] which can be easily accommodated in the monoxide crystal structure. Indeed, when the thermal treatment is carried out in Ar atmosphere, no trivalent cations are formed upon heating in the CP sample, all cations remaining in their initial divalent state. Therefore, one can argue that ϵ effect is associated with the reduction of $3+$ cations

formed during the thermal treatment in air, only; this accounts for molecular oxygen evolution, weight loss and the endothermic effect.

Conversely, DTA-DTG curves for HT sample are characterized by the presence of an endothermic peak at about 780°C paired with a modest weight loss both in air and Ar (Figure 5(b)). The different thermal behavior of HT and CP powders in argon can be explained by considering the pre-existing presence into the as-synthesized HT sample of Co₃O₄-like spinel (Figure 1). Therefore, the starting HT material is already characterized by the presence of 3+ cations prior to the thermal treatment, whose high temperature reduction causes η effect. One can additionally observe that η is less pronounced in Ar than in air atmosphere, this being correlated to the fact that the absence of O₂ upon heating in Ar does not allow further oxidation of other divalent cations.

Finally, at higher temperature (Figure 3, Table I), both materials appear to be constituted by the single-phase MgO-like rock salt structure, typical for this class of E-SO. The hydrothermal synthesized material shows almost perfect crystallization, all the diffraction peaks appearing very sharp (Figure 3(b)). Conversely, CP powder XRD pattern is characterized by evident peak broadening of the (2 0 0), (2 2 0) and (3 1 1) reflections, whereas (1 1 1) and (2 2 2) reflections do not show any relevant broadening (Figure 3(a)). Such phenomenon is known as anisotropic peak broadening, it taking place only on some specific crystallographic planes. It can be due to anisotropy in the crystallite size (i.e. the crystallite size is different on different crystallographic directions) or to the presence of anisotropic lattice strains due to anisotropic lattice disorder. As observed in Ref. [5], anisotropic broadening (in the form of reduction in the coherence length perpendicular to the (111) direction) is often observed in this class of materials and it is likely originated by short-distance displacements of the cations/oxygen in the lattice with respect to their ideal position. In order to characterize the observed behavior, a Popa-Balzar crystallite size/strain model was introduced in the Rietveld refinement [26], assuming pure strain-broadening hypothesis, with negligible size-related effects (i.e. no anisotropic broadening associated to the

crystallite shape). The absence of relevant anisotropy due to the crystallite shape is consistent with the high symmetry of fcc rock salt phase and it is confirmed by SEM micrographs, which will be discussed in “3.2 Sintering”, pointing out a very equiaxial grain structure. The refined values for the Popa strain coefficients are 0.5% for the average lattice strain and -0.4% along the cell diagonal direction. Such strains can adequately model the absence of broadening for the { 1 1 1} reflections and remarkable broadening effects in the others.

The different lattice strain behavior exhibited by HT and CP samples is thought to be associated with differences in the materials composition. Therefore, the chemical composition of HT and CP powder was measured by ICP and the results are shown in Figure 6. One can observe that the two samples are significantly different, the measured composition of HT sample being very close to the nominal one; conversely, Mg^{2+} content in CP sample is about one third the nominal one. The observed different results are easily justifiable on the base of the solubility data. In fact, while transition metals carbonates and hydroxides are practically insoluble in water, magnesium hydroxide has limited solubility and magnesium carbonate is relatively soluble. Therefore, in the presence of K_2CO_3 as precipitating agent, the final solution pH was too low (around 9 as measured after the co-precipitation step, the carbonate anion being a weak base) to allow the complete magnesium precipitation as $Mg(OH)_2$. Conversely, the remaining transition metal cations almost completely co-precipitated because of the very low solubility product for hydroxides, carbonates and basic carbonates. On the other hand, by using NaOH as precipitating agent for the combined co-precipitation/hydrothermal treatment, the solution pH was high enough (around 13, being NaOH a strong base) to ensure that all cations precipitate as hydroxides or oxides. The result is consistent with previous findings by Sarkar et al., who pointed out that pH = 10 is high enough to allow a complete precipitation of Mg^{2+} [13].

Starting from these results, the differences in lattice strain in CP and HT powder can likely be ascribed to the different Mg load. Since the E-SO crystal structure is well approximated by MgO-

like crystal, more limited Mg load in CP sample causes higher substitutional disorder with respect to the hydrothermal case. Therefore, it increases the broadening along (2 0 0), (2 2 0) and (3 1 1) reflections, likely due to higher cationic site density along these crystallographic planes.

3.2 Sintering

Figure 7 shows the dilatometric behavior of CP and HT powders. The plots are referred to pellets produced using powder calcined at 450°C to allow complete removal of crystallization water and CO₂ (β and ζ effects in Figure 2) before the green component production and firing. This was done to avoid possible damages of the specimens upon the sintering treatment, the rapid evolution of gaseous species in the green body very likely causing defects. The diagrams point out that the two materials are characterized by significant shrinkage at relatively low temperature. In particular, the powder produced by co-precipitation starts to shrink at about 400°C and the sintering process is almost completed at 950°C. The consolidation process for the powder obtained by hydrothermal route starts at about 700°C and a consistent shrinkage (in the order of 25%) is recorded at 1100°C although the process is not completed.

The strain rate curves (Figure 7) point out that the sintering process consists of two fundamental events for both materials, occurring at about 610/770°C and 795/1060°C for the co-precipitated and hydrothermal powder, respectively. Such relatively complex dilatometric behavior is very likely associated to different phenomena taking place upon heating, namely densification, crystallizations and phase transitions. In particular, a certain correspondence can be identified between the shrinkage rate maxima at 610/770°C (co-precipitated) and 795°C (hydrothermal) and the transformations previously indicated as δ , ϵ and η (Figure 2). The shrinkage at higher temperatures for the hydrothermal powder (maximum at 1060°C) can be ascribed instead only to densification and sintering.

The excellent sinterability of the material is confirmed by SEM/density analysis carried out on pellets treated at 1050°C for 1.5 h. The micrographs reported in Figure 8 reveal a very dense microstructure for CP material with few well-distributed small pores, mainly located at the grain boundary. A lower densification level is observed in the hydrothermal powder, although the material appears homogeneous and well-consolidated. The density measurements are in agreement with the microstructural analysis, the relative bulk density being close to 97% and 91% for CP and HT samples, respectively. XRD spectra recorded on the sintered pellets point out that the manufactured materials are constituted by the desired single-phase rock salt structure, additionally confirming the anisotropic strain broadening effect in CP sample (Figure 9). Therefore, the synthesis and sintering procedure developed in the present work represents a huge improvement with respect to previous literature results, where density in the range of 75-80% was obtained [5, 10, 12]. Nevertheless, we can observe a limited asymmetry in the low-angle part of the peak of HT sample (Figure 9). This could be accounted for by the coexistence of a second MgO-like phase with slightly different (larger) lattice parameters, or, more likely, by a slight distortion in the cubic structure of the main MgO-like phase due to the presence of lattice disorder (probably introduced during the comminution of the sintered pellet). As a matter of fact, the presence of a secondary phase would cause an increasing peak-splitting and such effect can not be observed in the diffraction patterns in Figure 9, the presence of a secondary phase appearing unlikely.

Additional micrographs of the crystalline grains structure are reported in Figure 10. The micrographs, obtained on free surface after sintering, show that the grains are almost equiaxial and the grain size is about 3.2 and 2.0 μm for the co-precipitated and hydrothermal synthesized material, respectively. Some abnormal grains can be also detected in the co-precipitated material, whose size is approximately 5 μm .

The obtained results suggest that self-diffusion kinetics in the considered materials are extremely rapid at relatively low temperature. Moreover, such kinetics are faster in CP sample, it being

characterized by quicker densification and grain coalescence. This can be associated to the different composition of the two materials, which mainly defers for the Mg load. The effect of Mg on sintering and grain growth can be examined by considering the defect chemistry of the material. The rock salt phase is constituted by the combination of a closed-packed anionic and cationic sublattices. In such structures, the most common defects are Schottky pairs, constituted by anion and cation vacancies. Frenkel disorder, which requires the formation of interstitials, is instead less common, the well packed crystal structure being poorly able to accommodate interstitial ions [25]. Therefore, sintering rates are very likely controlled by vacancies diffusion.

Indeed, the self-diffusion kinetics of anions (O) and cations (M) depends on the intrinsic diffusivities of the corresponding vacancies ($D_{VO\cdot}$ and $D_{VM\cdot}$) and on the defect population. In fact, the self-diffusion coefficients (D_O^{self} and D_M^{self}) can be calculated as following:

$$D_O^{self} = [V_O^{\cdot\cdot}] D_{VO\cdot} \quad \text{Eq.3}$$

$$D_M^{self} = [V_M^{\prime\prime}] D_{VM\cdot} , \quad \text{Eq.4}$$

where $[V_O^{\cdot\cdot}]$ and $[V_M^{\prime\prime}]$ are the concentration of anion and cation vacancies, respectively. On one hand the Mg load could interact with the intrinsic vacancies diffusivities. As a matter of fact, we observed that different Mg content is responsible for changes in the unit crystal cell, the cell parameter being 4.2442 Å and 4.2368 Å for the CP sample and HT sintered sample, respectively (calculated from XRD spectra in Figure 9). Therefore, the cell parameter is about 0.175% smaller in HT sample (with higher Mg load). The modification of the crystal structure indeed changes the vacancies diffusivities.

On the other hand, one can propose that the different Mg content influences the defect population. Many transition metal oxides with rock salt structure (Co and Ni, among them) have a strong tendency to non-stoichiometry due to the cation propensity to modify the oxidation state

from 2+ to 3+ [25]. This cation oxidation state variation is accommodated in transition metal rock salt monoxides by the formation of cation vacancies (V_M'') [25] according to the equilibrium:



The electron holes (h^\cdot) are associated to divalent lattice cations [27], which increase their oxidation state to 3+. Therefore, one can argue that E-SO are themselves partially non-stoichiometric rock salt compounds and, for this reason, we limit the discussion only to Mg, Co and Ni which have the same crystal structure of E-SO. In the case of CoO and NiO, the non-stoichiometry is relatively strong, it being in the order of 10^{-2} and 10^{-4} per cation sublattice site, respectively ($T \sim 1200^\circ\text{C}$ and $P_{O_2} \sim 0.2 \text{ atm}$) [28]. On the other hand, MgO is much more stoichiometric than NiO and CoO and the ionic vacancies concentration, according to Schottky equilibrium, is practically negligible at 1050°C (the intrinsic vacancies concentration is only $4 \cdot 10^{-7}$ even at melting temperature $\sim 2850^\circ\text{C}$ [25]). Therefore, the different composition of CP and HT powder can cause a substantial modification of the defects population, the latter being very likely more stoichiometric as a result of the larger Mg content.

4 Conclusions

(Mg, Co, Ni, Cu, Zn)O entropy-stabilized oxides can be successfully obtained by employing wet chemical synthesis methods like co-precipitation (using K_2CO_3 as precipitating agent) and hydrothermal synthesis. Albeit a certain deviation from the predicted stoichiometry is observed in the co-precipitated sample, both produced materials are constituted by the desired single-phase solid solution with rock salt structure.

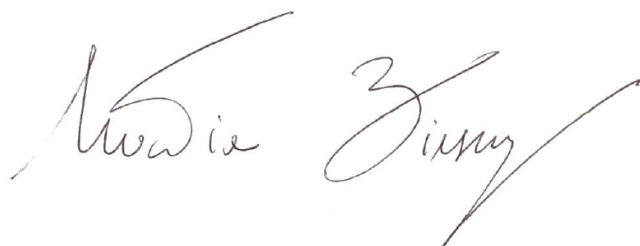
The obtained powders are characterized by an excellent sinterability, which allows the production of well-consolidated pellets at relatively low temperatures (1050°C), the relative density of the fired samples being $\sim 97\%$ and $\sim 91\%$ for CP sample and HT sample, respectively.

Compliance with Ethical Standards

Funding: This study was not funded by any institution.

Conflict of Interest: Authors have not received any grants. The authors declare that they have no conflict of interest.

Mattia Biesuz on behalf of all authors

A handwritten signature in black ink, appearing to read "Mattia Biesuz". The signature is written in a cursive, flowing style.

References

1. Rost CM, Sachet E, Borman T, et al (2015) Entropy-stabilized oxides. Nat Commun 6:8485
2. Rak Z, Rost CM, Lim M, et al (2016) Charge compensation and electrostatic transferability in three entropy-stabilized oxides: Results from density functional theory calculations. J Appl Phys 120:95105
3. Rost C (2016) Entropy-Stabilized Oxides: Explorations of a Novel Class of Multicomponent Materials. North Carolina State University
4. Rost CM, Rak Z, Brenner DW, Maria J-P (2017) Local structure of the $Mg_x Ni_x Co_x Cu_x Zn_x O$ ($x=0.2$) entropy-stabilized oxide: An EXAFS study. J Am Ceram Soc 2732–2738
5. Berardan D, Meena AK, Franger S, et al (2017) Controlled Jahn-Teller distortion in

(MgCoNiCuZn)O-based high entropy oxides. *J Alloys Compd* 704:693–700

6. Ragone D V. (1995) *Thermodynamic of Materials*, Vol.2. Wiley
7. Yalamanchili K, Wang F, Schramm IC, et al (2017) Exploring the high entropy alloy concept in (AlTiVNbCr)N. *Thin Solid Films* 636:346–352
8. Gild J, Zhang Y, Harrington T, et al (2016) High-Entropy Metal Diborides: A New Class of High-Entropy Materials and a New Type of Ultrahigh Temperature Ceramics. *Sci Rep* 6:37946
9. Brenner D, Maria J, Opila B, et al (2015) The Science of Entropy Stabilized Ultra-High Temperature. <https://research.mse.ncsu.edu/entropysciencemuri/wp-content/uploads/sites/7/2016/08/NSMMS-Brenner.pdf>
10. Bérardan D, Franger S, Meena AK, Dragoe N (2016) Room temperature lithium superionic conductivity in high entropy oxides. *J Mater Chem A* 4:9536–9541
11. Djenadic R, Sarkar A, Clemens O, et al (2017) Multicomponent equiatomic rare earth oxides. *Mater Res Lett* 5:102–109
12. Bérardan D, Franger S, Dragoe D, et al (2016) Colossal dielectric constant in high entropy oxides. *Phys Status Solidi - Rapid Res Lett* 10:328–333
13. Sarkar A, Djenadic R, Usharani NJ, et al (2017) Nanocrystalline multicomponent entropy stabilised transition metal oxides. *J Eur Ceram Soc* 37:747–754
14. Spiridigliozzi L, Dell'agli G, Biesuz M, et al (2016) Effect of the Precipitating Agent on the Synthesis and Sintering Behavior of 20 mol % Sm-Doped Ceria. *Adv Mater Sci Eng* 2016:6096123
15. Lutterotti L, Bortolotti M, Ischia G, et al (2007) Rietveld texture analysis from diffraction

images. Zeitschrift fur Krist Suppl 1:125–130

16. Ayask HK, Khaki JV, Haddad Sabzevar M (2015) Facile synthesis of copper oxide nanoparticles using copper hydroxide by mechanochemical process. *J Ultrafine Grained Nanostructured Mater* 48:37–44
17. Wang B, Lu X-Y, Tang Y (2015) Synthesis of snowflake-shaped Co_3O_4 with a high aspect ratio as a high capacity anode material for lithium ion batteries. *J Mater Chem A* 3:9689–9699
18. Abbas SA, Jung KD (2016) Preparation of mesoporous microspheres of NiO with high surface area and analysis on their pseudocapacitive behavior. *Electrochim Acta* 193:145–153
19. Dong H, Unluer C, Yang EH, Al-Tabbaa A (2017) Synthesis of reactive MgO from reject brine via the addition of NH_4OH . *Hydrometallurgy* 169:165–172
20. Shaporev AS, Ivanov VK, Baranchikov AE, et al (2007) ZnO formation under hydrothermal conditions from zinc hydroxide compounds with various chemical histories. *Russ J Inorg Chem* 52:1811–1816
21. Brown IWM, Mackenzie KJD, Gainsford GJ (1984) Thermal decomposition of the basic copper carbonates malachite and azurite. *Thermochim Acta* 74:23–32
22. El-Shobaky GA, Ahmad AS, Al-Noaimi AN, El-Shobaky HG (1996) Thermal decomposition of basic cobalt and copper carbonates. *J Therm Anal* 46:1801–1808
23. Kissinger HE (1957) Reaction Kinetics in Differential Thermal Analysis. *Anal Chem* 29:1702–1706
24. Mittemeijer EJ (1992) Review - Analysis of the Kinetics of Phase Transformations. *J Mater Sci* 27:3977–3987

25. Chiang Y-M, Birnie D, Kingery PWD (1997) Physical Ceramics: Principles for Ceramic Science and Engineering. Wiley
26. Popa NC (1998) The (hkl) Dependence of Diffraction-Line Broadening Caused by Strain and Size for all Laue Groups in Rietveld Refinement. J Appl Crystallogr 31:176–180
27. Kingery WD, Bowen HK, Uhlmann DR (1976) Introduction to Ceramics, Second. Wiley, New York (USA)
28. Peterson NL (1984) Point Defects and Diffusion Mechanisms in the Monoxides of the Iron-Group Metals. Mater Sci Forum 1:85–107

Table I: Mineralogical composition calculated by Rietveld method (using Maud software) from the spectra in Figure 3.

	T [°C]	Rock salt [wt%]	Spinel [wt%]	Zinc oxide [wt%]	Tenorite [wt%]
CP	520	32.0	50	4	14
	690	87	0	4	9
	1000	100	0	0	0
HT	700	69	9	5	17
	920	98	0	2	0
	1000	100	0	0	0

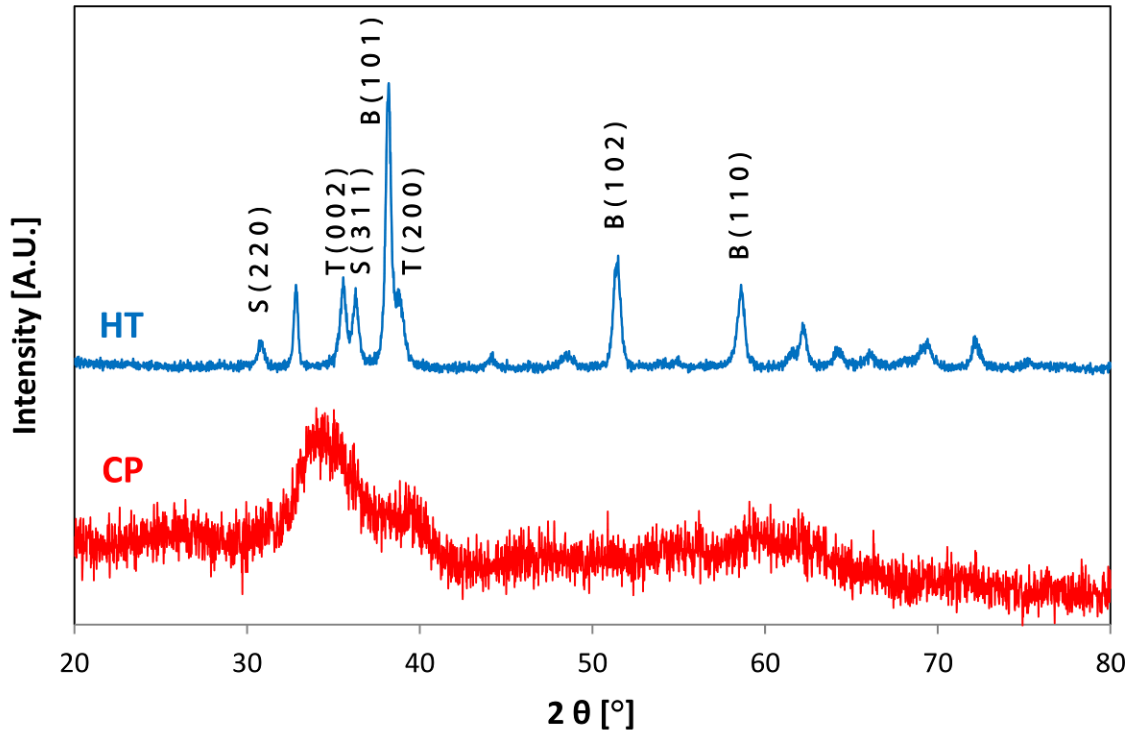


Figure 1: XRD spectra of powders synthesized by co-precipitation (CP) and hydrothermal process (HT). Crystalline phases and corresponding reflexes in HT powder are indicated: brucite (B), cobalt oxide spinel (S) and tenorite (T).

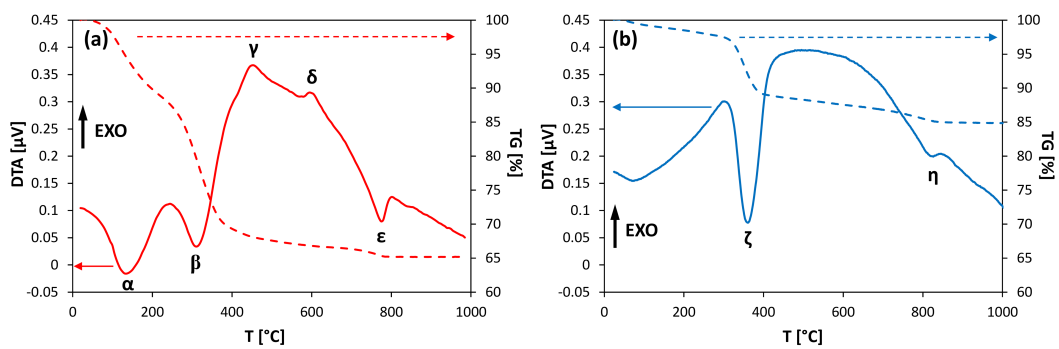


Figure 2: TG/DTA plots of powders synthesized by co-precipitation (a) and by hydrothermal synthesis (b).

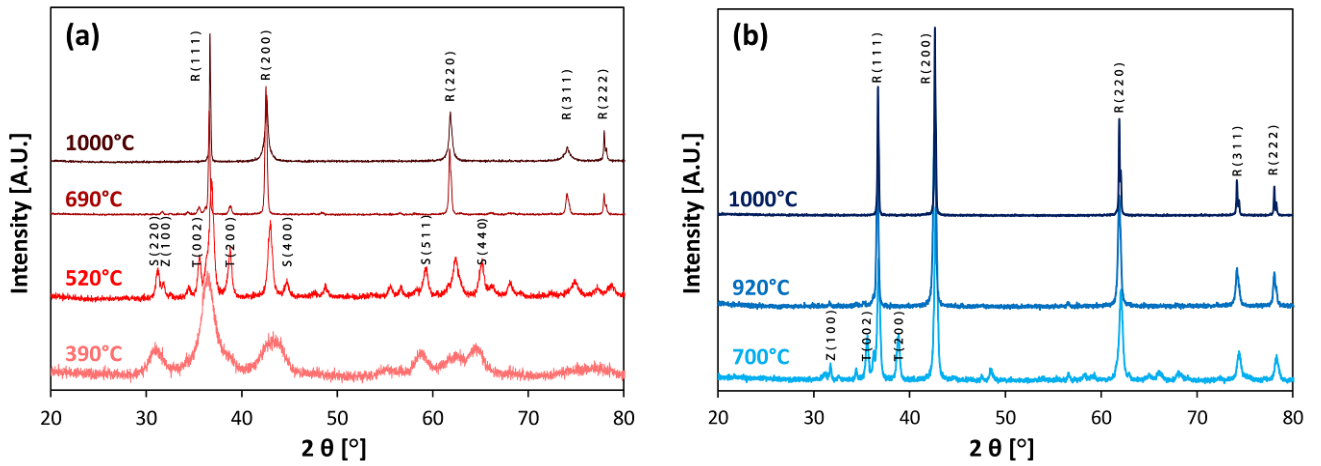


Figure 3: XRD spectra of co-precipitated (a) and hydrothermal synthesized powder (b) after calcination at specific temperature and successive quenching. Crystalline phases and corresponding peaks are indicated: rock salt MgO-like (R), cobalt oxide spinel (S), zinc oxide (Z) and tenorite (T).

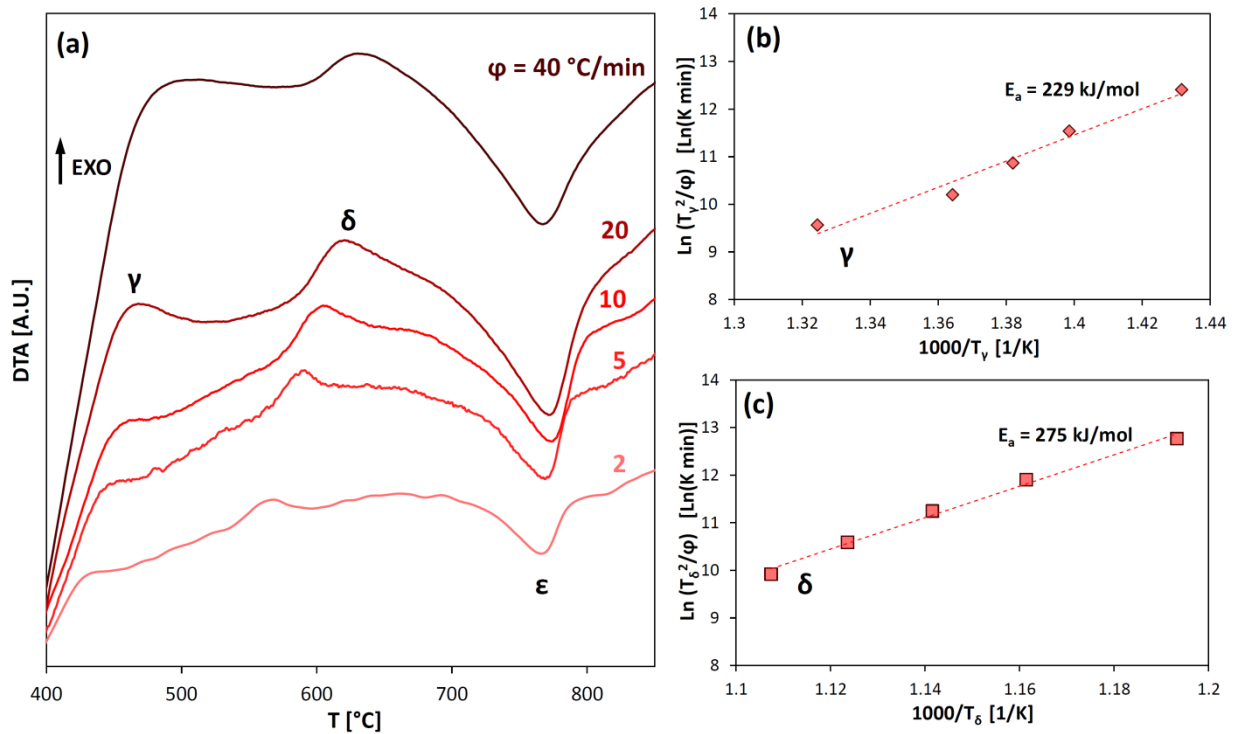


Figure 4: DTA plots recorded using different heating rates on the material produced by co-precipitation (a). Linearization of the relation between DTA peak temperature and heating rate (Eq. 2) for γ (b) and δ (c) transformations.

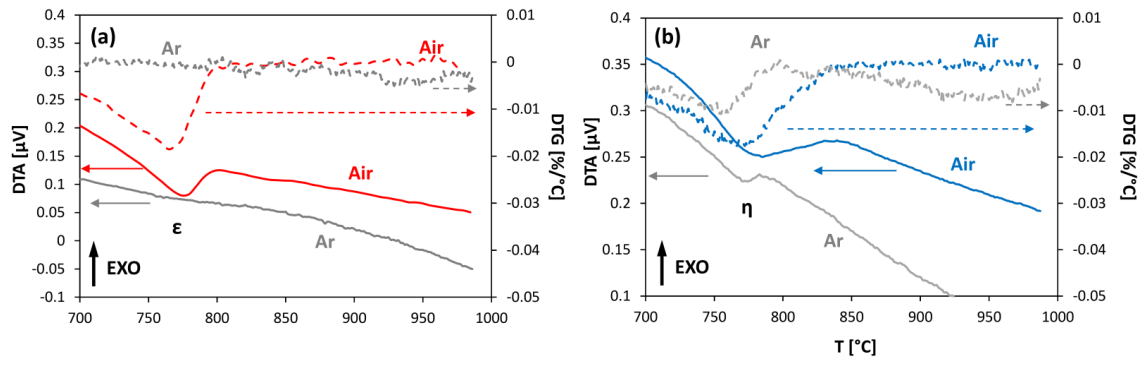


Figure 5: DTA-DTG taken on CP (a) and HT (b) powders in Ar and air atmosphere.

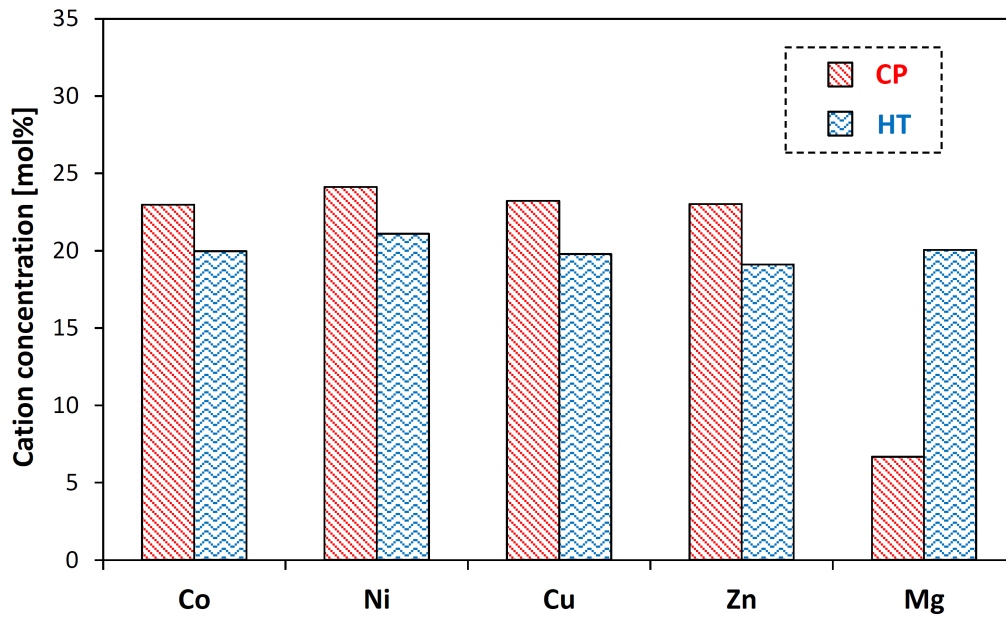


Figure 6: Cation concentrations determined by ICP on the calcined powders (450°C, 1 h).

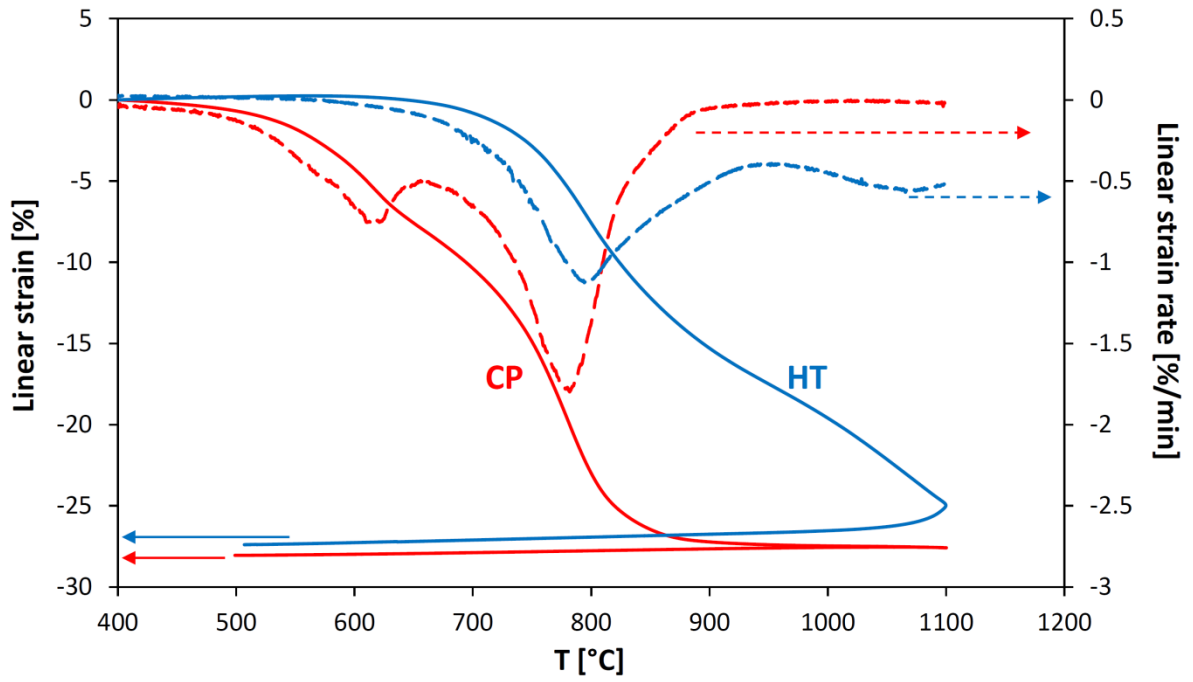


Figure 7: Linear deformation and corresponding derivative from dilatometric analysis carried out up to 1100°C on calcined powder pellets (heating rate = 10°C/min).

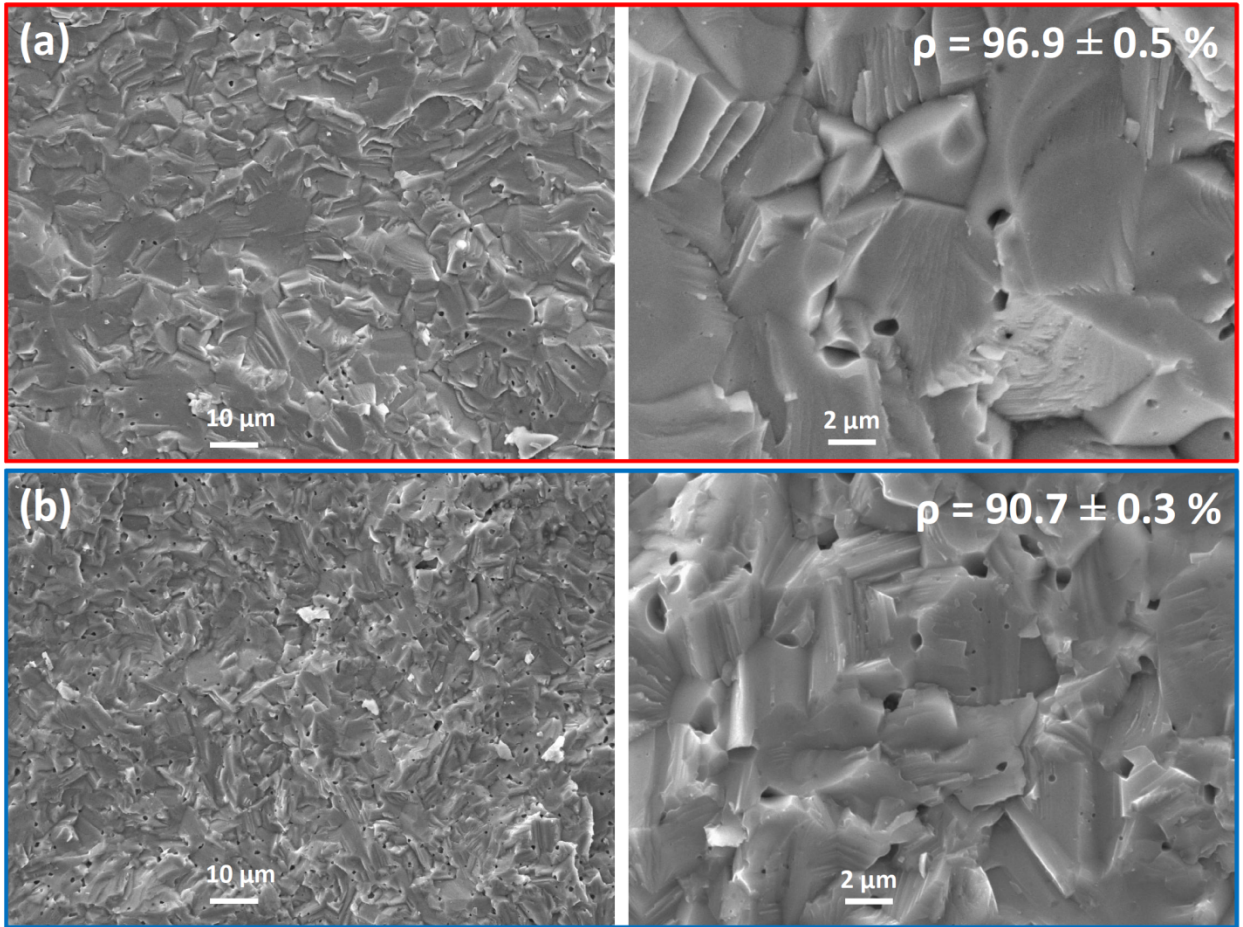


Figure 8: SEM micrographs of sintered pellets fracture surface: co-precipitated (a) and hydrothermal synthesized (b) powder.

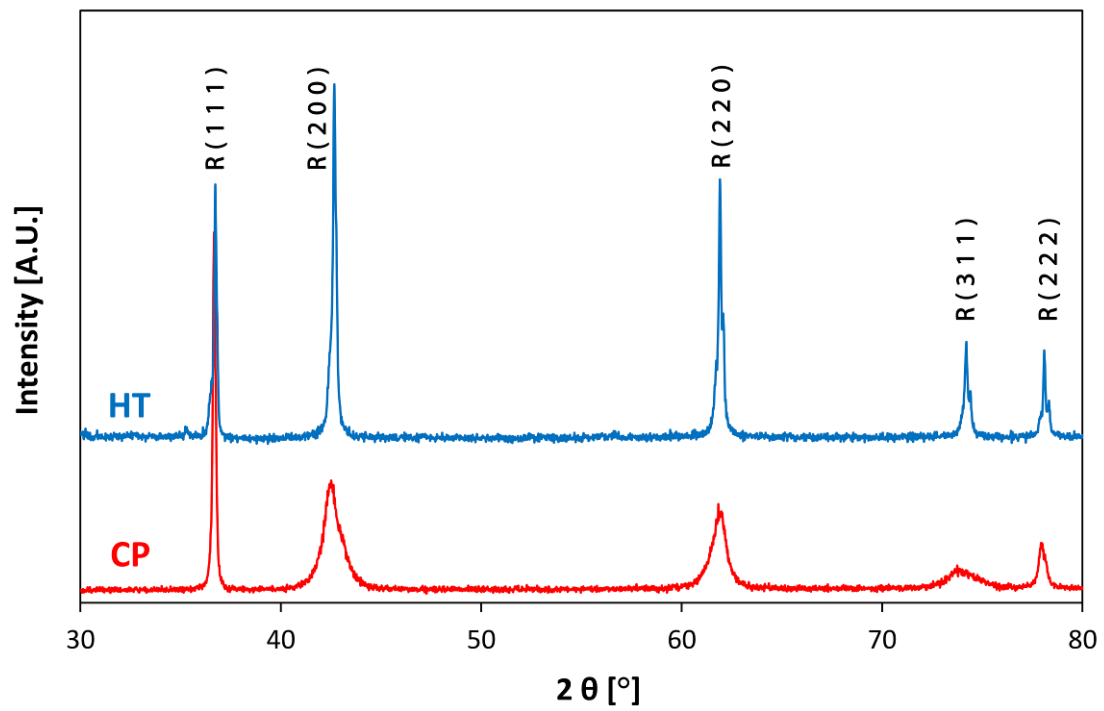


Figure 9: XRD spectra obtained on ground sintered pellets (1050°C, 1.5 h).

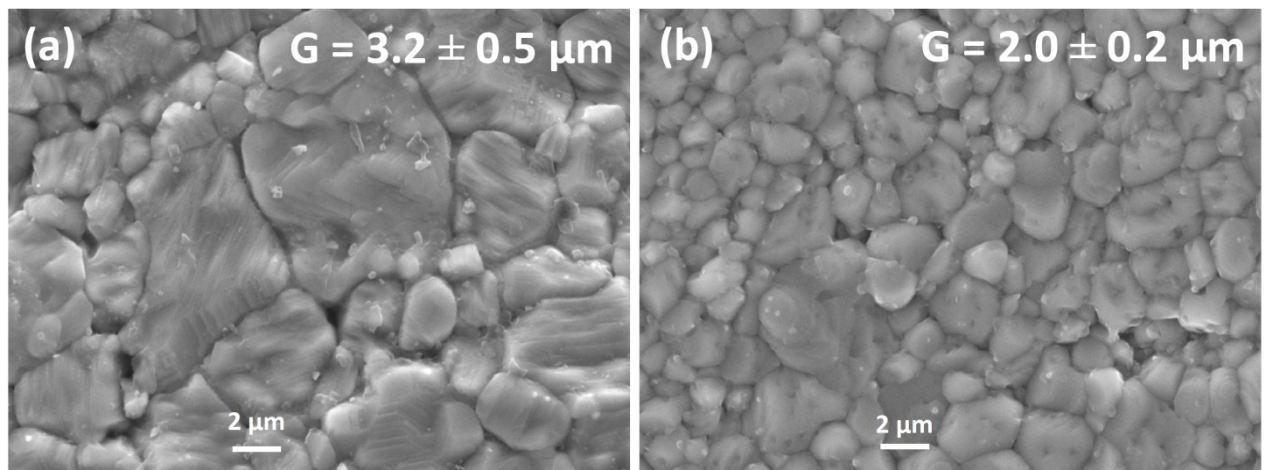


Figure 10: SEM micrographs of the sintered pellets free surface: co-precipitated (a) and hydrothermal synthesized (b) powder.